ASTROBIOLOGY
Volume 8, Number 5, 2008

DOI: 10.1089/ast.2007.0142

Special Paper

The MARTE VNIR Imaging Spectrometer Experiment: Design and Analysis

Adrian J. Brown,[1,2] Brad Sutter,[2,*] and Stephen Dunagan[2]

Abstract

We report on the design, operation, and data analysis methods employed on the VNIR imaging spectrometer instrument that was part of the Mars Astrobiology Research and Technology Experiment (MARTE). The imaging spectrometer is a hyperspectral scanning pushbroom device sensitive to VNIR wavelengths from 400–1000 nm. During the MARTE project, the spectrometer was deployed to the Río Tinto region of Spain. We analyzed subsets of 3 cores from Río Tinto using a new band modeling technique. We found most of the MARTE drill cores to contain predominantly goethite, though spatially coherent areas of hematite were identified in Core 23. We also distinguished non Fe-bearing minerals that were subsequently analyzed by X-ray diffraction (XRD) and found to be primarily muscovite. We present drill core maps that include spectra of goethite, hematite, and non Fe-bearing minerals. Key Words: Mars—Analogue—Río Tinto—Reflectance spectroscopy—Infrared spectroscopy. Astrobiology 8, xxx–xxx.

Introduction

In September of 2005, remote subsurface drilling procedures were tested in the Río Tinto region of Spain, as a precursor to drilling on Mars. The experiment package, known as the Mars Astrobiology Research and Technology Experiment (MARTE), consisted of a remotely operated drilling platform and associated instruments that examined retrieved drill cores. One of the instruments on board the drilling rig was a Visible–Near Infrared (VNIR: 400–1000 nm) imaging spectrometer. Here, we describe the design and operation of the imaging spectrometer and how the VNIR imaging spectrometer data were analyzed. We present the results of analyzing subsets of 3 cores from the MARTE robotic drilling project.

The MARTE Project

The MARTE project was conceived, planned, and executed in 2003–2005, and the remote science experiment took place in September 2005 (see Stoker *et al*., 2008). MARTE was conceived as a high-definition simulation of remote drilling on the martian surface with the intent to identify subsurface life. Several instruments were mounted on a drill rig to analyze cores remotely and upon extraction. In addition to the VNIR imaging spectrometer described herein, the instrument suite included a Raman spectrometer, a VNIR point spectrometer (Sutter *et al*., 2008), and several organic analysis devices (Stoker *et al*., 2008).

The MARTE project was conducted in the Río Tinto region of the Iberian pyrite belt in southern Spain as an analog site for Mars. The Río Tinto region is unique due to the unusual preponderance and diversity of iron-rich minerals formed in and on the periphery of the Río Tinto river, which is colored deep red as a result. This unusual situation is caused by hydrothermal activity linked to the Hercynian orogeny (Schermerhorn, 1970). Hydrothermal waters coursed through Devonian to Carboniferous volcanics and created the subvolcanic Iberian pyrite belt. Later orogenesis exposed the pyrite to surface water, and microbially mediated oxidation produced an acid sulfate environment in which minerals such as jarosite, hematite, goethite, barite, and more exotic Fe oxides, Fe oxyhydroxides, and Fe sulfate hydrates have precipitated (Fernández-Remolar *et al*., 2003). The Río Tinto oxidized Fe mineralogy is similar to that found on Mars; however, we do not take this as an indication that Fe oxides on Mars must be mi-

[1]SETI Institute, Mountain View, California.
[2]Ames Research Center, Moffett Field, California.
*Present address: Jacobs NASA/JSC, Houston, Texas.

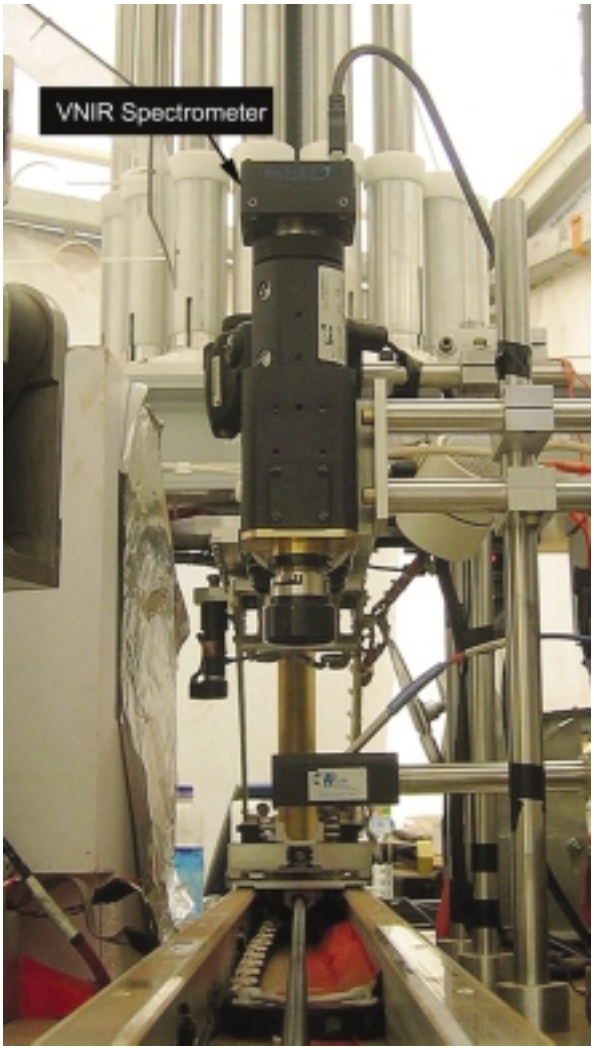

4C online B/W print

FIG. 1. The MARTE VNIR imaging spectrometer system mounted on the drill core bench. The vertical black spectrometer housing is approximately 15 cm high.

crobially mediated. Nevertheless, we do believe the mineral suite available at the Río Tinto serves as an analogue by which to test technologies and instrumentation intended for Mars (Fernández-Remolar *et al.*, 2005).

MARTE VNIR Imaging Spectrometer

The MARTE VNIR imaging spectrometer system shown in Fig. 1 was developed at NASA Ames Research Center. The imaging spectrometer was included as part of the drill-core analysis suite on a Mars analog life-detection mission—not as a direct indicator of life but to give mineralogical context to other instruments.

The spectrometer incorporates an imaging spectrometer and monochrome industrial vision CCD camera in a scanning configuration, which permits high-resolution imaging of rock core samples with a high degree of spectral information (Hyvarinen *et al.*, 1998). The instrument utilizes macroscopic imaging optics and a slit input aperture to sample a line on the object (core). Scanning the core along its axis (normal to the slit) while taking multiple images generates a data "hypercube" in the mode of classic "pushbroom" type remote sensing instruments [*e.g.*, PHILLS, HYDICE (Kappus *et al.*, 1996; Davis *et al.*, 2002)].

The spectrometer operates under controlled illumination, and a spectral calibration is performed by way of vapor emission lamps. Radiometric calibration is achieved by a uniform Spectralon® calibration target in the object field. A "quick-look" color image is produced at the end of the scan, which is comprised of 3 wavelength bands that represent normal human perception of blue (480 nm), green (530 nm), and red (660 nm). The instrument operator may specify regions of interest in the quick-look image and load a request to the hypercube data mining software, which will return reflectance spectra data averaged over these regions.

Principles of operation

The optical system is depicted in Fig. 2, with rays tracing the propagation of blue, red, and infrared light (shown as purple in the figure). The objective focuses the target object (in this case the surface of the core) onto a slit input aperture. Light passing through the slit is collimated, refracted by a wedge prism, and directed to a diffraction grating. The first-order diffracted light from the grating is passed through another wedge prism and focused by a second infinite-conjugate-ratio lens to an array detector. A dichroic order-blocking filter (obf) is mounted in front of the CCD to eliminate interference from zero or second-order diffraction.

This optical system has the effect of spectrally dispersing the light across one dimension of the array detector. The confocal collimating lenses inside the spectrometer relay the slit image to the other (spatial "cross scan") dimension of the array detector, which provides an image of a line from the object. The second spatial dimension of the hypercube is scanned out by taking sequential spectral frames while linearly translating the spectrometer with respect to the target object at constant focal range in a direction normal to the slit orientation. This was accomplished by way of the transla-

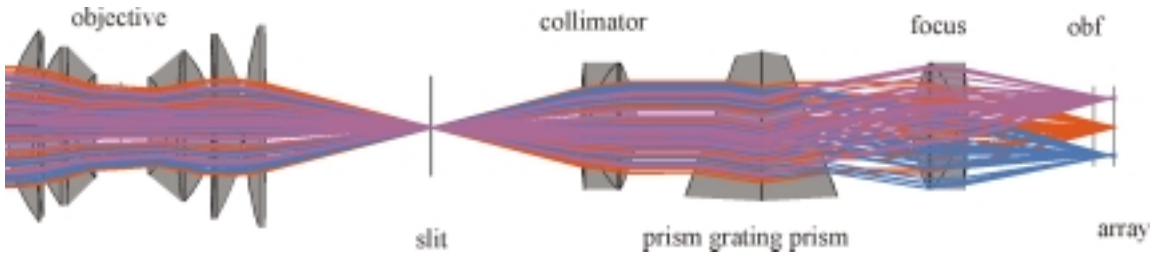

4C online B/W print

FIG. 2. The MARTE VNIR imaging spectrometer optical system diagram.

TABLE 1. MARTE VNIR IMAGING SPECTROMETER SYSTEM SPATIAL SAMPLING CHARACTERISTICS

	Cross scan direction	*Along scan direction*
Spatial resolution at detector	8.3 μm (CCD pixel size limited)	13 μm (slit width limited)
Spatial resolution at core (f = 17 mm, magnification = 0.25)	50 μm	81 μm
Spatial sampling interval of scanner		50 μm

tion mechanism of the MARTE core processing system. The scan parameters (speed, frame rate) were controlled to move the spectrometer a distance equal to the "cross-scan" pixel size in object space in order to have "square" pixels in the hypercube.

Design features

The imaging characteristics of the spectrometer are determined by several optical design choices. The input slit aperture is 13 μm wide. The array detector was oriented with its longer dimension spanning the spectral dimensions of the image plane to achieve the maximum spectral range. The array comprises a Sony ICX 415AL/AQ progressive scan CCD chip that has 782 by 582 effective pixels, an 8 mm diagonal (Type 1/2'), and a unit cell size of 8.3 μm by 8.3 μm. The spectrometer collimating and focal lenses provide unmagnified imaging of the slit to the array detector in the spatial dimension; therefore, the instantaneous spatial pixel dimension is 13 μm along track by 8.3 μm cross track, times the magnification ratio of the objective (Table 1). A fixed-focus (infinite conjugate) objective lens with 17 mm focal length was selected to provide appropriate magnification of the 27 mm core diameter across the full spatial dimension of the array detector (Table 1). This spatial resolution is further elongated in the track direction by the product of scan-speed and camera shutter exposure time; however, this effect is negligible for the slow scan speeds used in this experiment.

In our study, the spectrometer resolved 580 columns of 50 μm spatial elements along the input aperture. A 50 μm spatial size pixel was chosen to be a reasonable fit to the expected mineral grain size. The hypercube image length was specified by the length of the scan, configured for rock cores 25 cm long with 1 cm of overlap on either end. The spectrum was sampled by 780 detector rows that span the 400–1000 nm wavelength range. The 780 rows were binned into six-pixel averages for a total of 130 final bands. The hypercubes produced in this experiment can be visualized as a stack of monochrome images of increasing wavelength as one "drills down" through the stack. In fact, the vertical data distribution represents the reflectance spectrum for a particular pixel on the core surface. All hypercubes were of identical dimensions—5221 pixels long by 580 pixels wide and with 130 spectral channels.

The camera well depths and analog-to-digital converters limit signal to 8 bits of discrimination at peak intensity, occurring near the green portion of the spectrum. Reflectance measurements are considerably degraded at the long- and short-wave ends of the spectral range by a combination of (1) reduced quantum efficiency in silicon and (2) reduced illumination power in the shortwave end of the tungsten-halogen illumination lamp spectrum. To address this problem, an amethyst filter was used to suppress the green peak in the detector response, which permits the use of longer integration times to increase the blue and infrared signal strength without saturating the green wavelengths. These effects are depicted in Fig. 3. Normalized curves for detector response, lamp illumination (color temp = 3000 K), and filter pass are shown in Fig. 3a. Figure 3b shows the spectral response of the instrument, which results from the combination of these

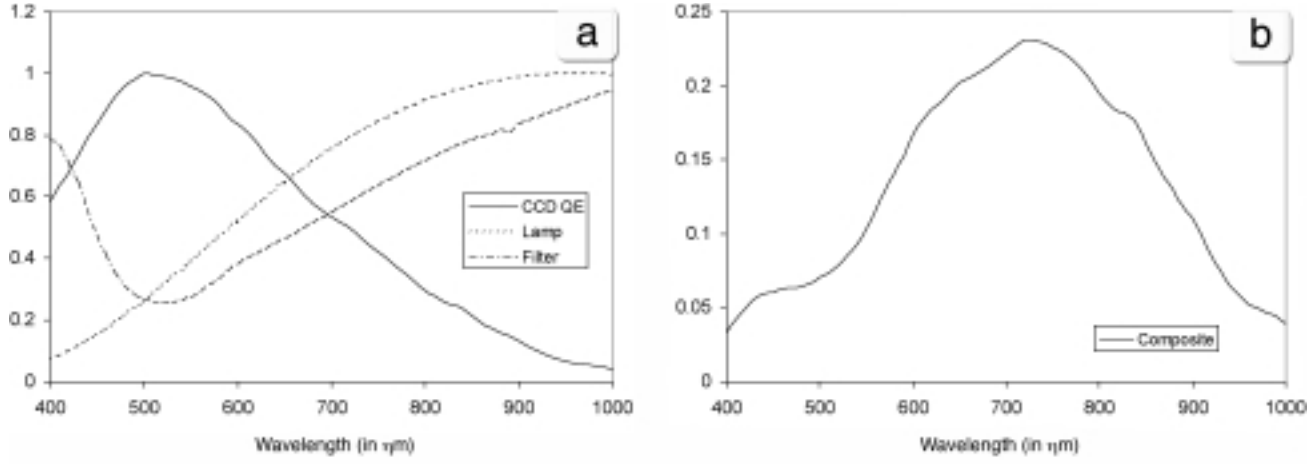

FIG. 3. Spectral calibration curves. (**a**) CCD quantum efficiency, lamp intensity, and filter spectral curve. (**b**) Calculated spectrometer radiometric response function.

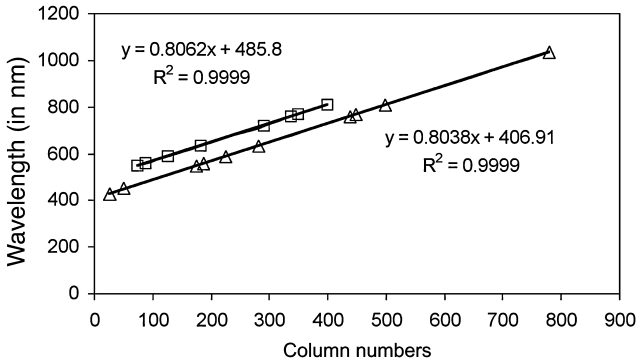

FIG. 4. Spectral calibration curves for measurements of the Krypton emission lines for orthogonal orientations of the array detector. Squares are for the short dimension and triangles are for the long dimension of the rectangular detector (the long dimension was used in the field instrument).

effects and illustrates the loss of dynamic range and signal at the ends of the spectrum.

The VNIR imager provides a high degree of flexibility in adapting the sensor to a specific measurement problem (both in design and during operation). The diffractive spectral resolution of the instrument is 2.8 nm and is over-sampled by a factor of 4 at the array detector. The full hypercube may be reduced by averaging (in real time) over adjacent spectral rows, down to the spectral resolution required for the experiment. This permits customized attention to specific spectra, reduces the data to a more manageable volume, and enables faster sampling. The averaging process also improves the signal-to-noise ratio of the instrument. The repetitive nature of the scanning process, along with remote control over the illumination and data mining operations, made this instrument a good match to the robotic experimental design.

Calibration

Pre-scan calibrations provide spectral calibration data to convert CCD columns to wavelength, as well as dark frame and normalization frame data that are useful in converting measured radiance to reflectance. Sample spectral calibration data are presented in Fig. 4. These curves are computed by way of the known emission lines of gas discharge lamps—in this case xenon, krypton, mercury, and neon lines. The two curves shown on Fig. 4 are derived from orienting the array detector to measure dispersion along either the short (square symbols) or long (triangle symbol) dimension of the rectangular array detector. The long dimension is the one used in this application, which provides spectral coverage from about 400 to over 1000 nm (over 780 columns binned to 130 columns). When spectral compression is used, the slope of the wavelength calibration curve of Fig. 4 is multiplied by the compression factor, and the *y*-intercept is slightly shifted as a result.

We used a krypton lamp as a test target to check the spectral linearity and accuracy of our instrument. We verified that the spectrometer bands were accurate to within 5 nm across the full range of the instrument, which was deemed sufficient for the purposes of this investigation. An example of a sample normalization frame acquired over a fully illuminated Spectralon® reflectance target is presented in Fig. 5. Note the high correlation with the calculated response curve shown in Fig. 3b. Some vignetting effects may be seen in the upper and lower parts of the frame but are limited to intensity error only, since the emission lines are straight to within one pixel variation across the detector. This is a systematic error, which may be corrected with the previously described radiometric calibration procedure.

The reflectance value of the calibration target (R_{cal}) may be adjusted to maximize the dynamic range of the spectrometer over the reflectivity range of the samples. With this approach, when portions of the sample reflect greater than the R_{cal} value, the sensor will saturate and data from those pixels will be compromised. For this experiment, an R_{cal} of 75% was used in order to avoid such saturation conditions. A current-controlled (less than 0.5% variation) tungsten-halogen light source was chosen to provide high reflected light levels (particularly in the infrared) and stable illumination. Camera settings are optimized to provide the desired gain and integration time (generally as long as possible without causing excessive scan time) to yield maximum intensities reflected from the calibration target just under the saturation level of the camera.

To convert the raw digital number values from the camera to calibrated reflectance values, we evaluated Eq. 1 over every element of the 3-D hypercube array.

$$R_{Measured} = R_{cal} \cdot \frac{(DN_{measured} - DN_{DarkCal})}{(DN_{WhiteCal} - DN_{DarkCal})} \quad (1)$$

where DN stands for digital number (ranging 0–255 for a camera in 8-bit mode) and $DN_{WhiteCal}$ and $DN_{DarkCal}$ are the values in the corresponding pixel locations in the reference and dark calibration frames. This simple data-processing approach relies on stability of the sensitivity of the CCD (typically requiring stable temperature) and uniform lighting conditions over the period from calibration to measurement. For the MARTE project, a reflectance standard was measured at the beginning of each new core.

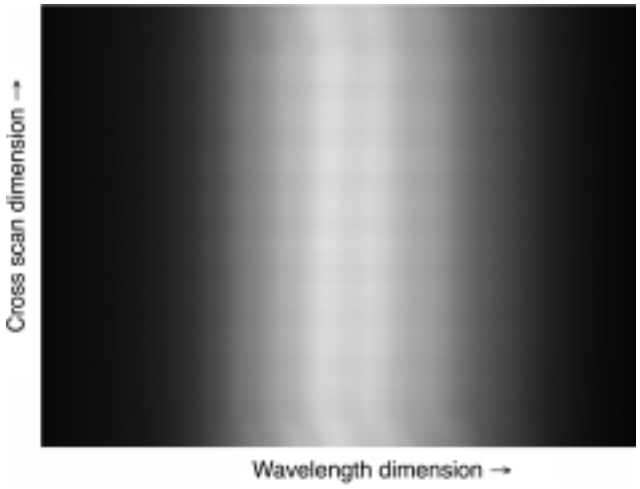

FIG. 5. Measured sample normalization frame of a fully illuminated Spectralon® plate.

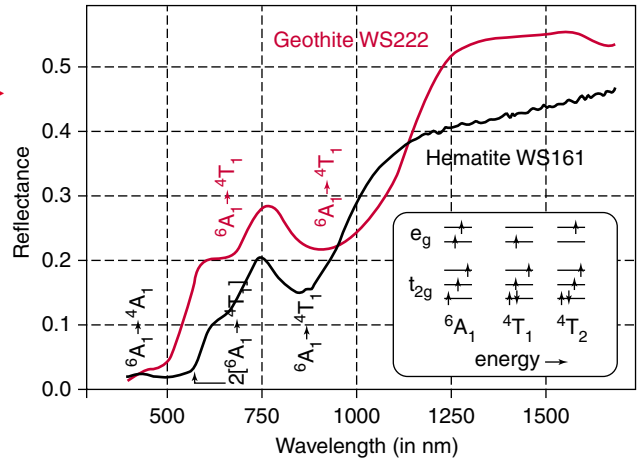

FIG. 6. VNIR spectra of hematite and goethite from the USGS Mineral Library (Clark *et al.*, 2003) and crystal field theory energy diagrams for the 3 lowest-energy spin-orbital states of tetrahedrally coordinated Fe^{3+}. Octahedrally coordinated Fe^{3+} spin-orbital states are the same but require the addition of a g subscript to designate centrosymmetric coordination sites.

Analysis of Hyperspectral Images

Crystal field theory background

Crystal field theory is a method by which the electron energy gaps can be estimated from knowledge of the structure of a mineral; it was pioneered by Hans Bethe (Bethe, 1927). Crystal field theory gives us a qualitative understanding of infrared spectra of transition metal–bearing compounds in the 400–1000 nm wavelength range. Transition metals are those elements with a partly filled d or f shell. Several absorption bands due to d shell electron promotion in transition metals are present in the 400–1000 nm wavelength range (Hunt, 1977).

For this study, we were principally concerned with ferric (Fe^{3+}) iron–bearing minerals—specifically hematite (α-Fe_2O_3) and goethite (α-FeOOH). An isolated, unexcited Fe^{3+} ion has 23 electrons and a $3d^5$ electronic configuration—it requires 5 electrons to complete its d shell. A d shell has 5 orbitals (d_{xy}, d_{yz}, d_{xz}, d_{x2-y2} and d_{z2}); and in a free Fe^{3+} ion, a d-shell electron has an equal probability of occupying each d orbital (the orbitals are degenerate). The 5 orbitals are broken into 2 symmetry groups: t_{2g} for d_{xy}, d_{yz}, and d_{xz} and e_g for d_{x2-y2} and d_{z2}. When a transition ion is in a crystal structure, the effect of a non-spherical electrostatic field lowers this degeneracy and splits the d orbitals into different energies. The exact splitting depends on type, positions, and symmetry of ligands surrounding the transition metal (Burns, 1993).

When a transition ion is octahedrally coordinated, the 2 e_g orbitals point toward neighboring ligands and, therefore, are less stable than the 3 t_{2g} orbitals (this situation is reversed in cubic structures, for example).

The ground state Fe^{3+} ion in an octahedral crystal field can be represented as $^6A_{1g}$. The superscript 6 designates the spin-multiplicity of this state (a sextet in this case), which is obtained by adding one to the number of unpaired electrons. Thus $^6A_{1g}$ is a sextet state with five unpaired electrons with spins aligned parallel to each other (Fig. 6). Spin-allowed transitions occur between 2 states with the same spin multiplicity. All excited states of Fe^{3+} have lower spin-multiplicities than the ground state, which leads to weak "spin-forbidden" transitions. Thus, an octahedral Fe^{3+} transition from $^6A_{1g} \rightarrow {}^4T_{2g}$ is a spin-forbidden transition and is markedly weaker than the octahedral Fe^{2+} spin-allowed transition $^5T_{2g} \rightarrow {}^5E_g$, for example.

Ferric iron in goethite, nontronite, lepidicrocite, and jarosite is octahedrally coordinated. Consequently, each of these minerals has broad bands centered near 640 and 900 nm, corresponding to the energies for $^6A_1 \rightarrow {}^4T_2$ and $^6A_1 \rightarrow {}^4T_1$ spin-forbidden crystal field transitions (Fig. 6). Fe^{3+} in hematite is also octahedrally coordinated; however, it displays a greater intensity at 2 additional bands at 430 and 550

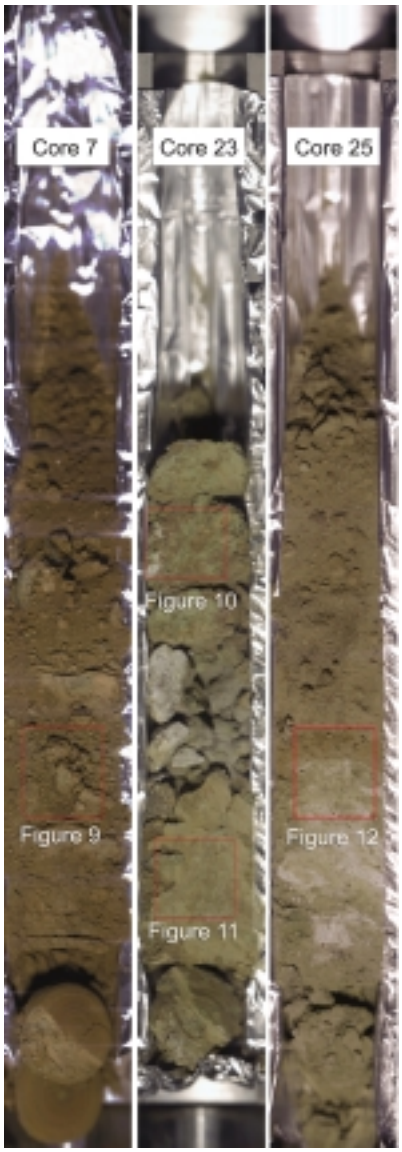

FIG. 7. Approximate true-color images (red = 660 nm, green = 616 nm, blue = 567 nm) of Cores 7, 23 and 25, showing locations mapped in Figs. 9–12. Each core is 27 mm in diameter (AQ series diamond drill core).

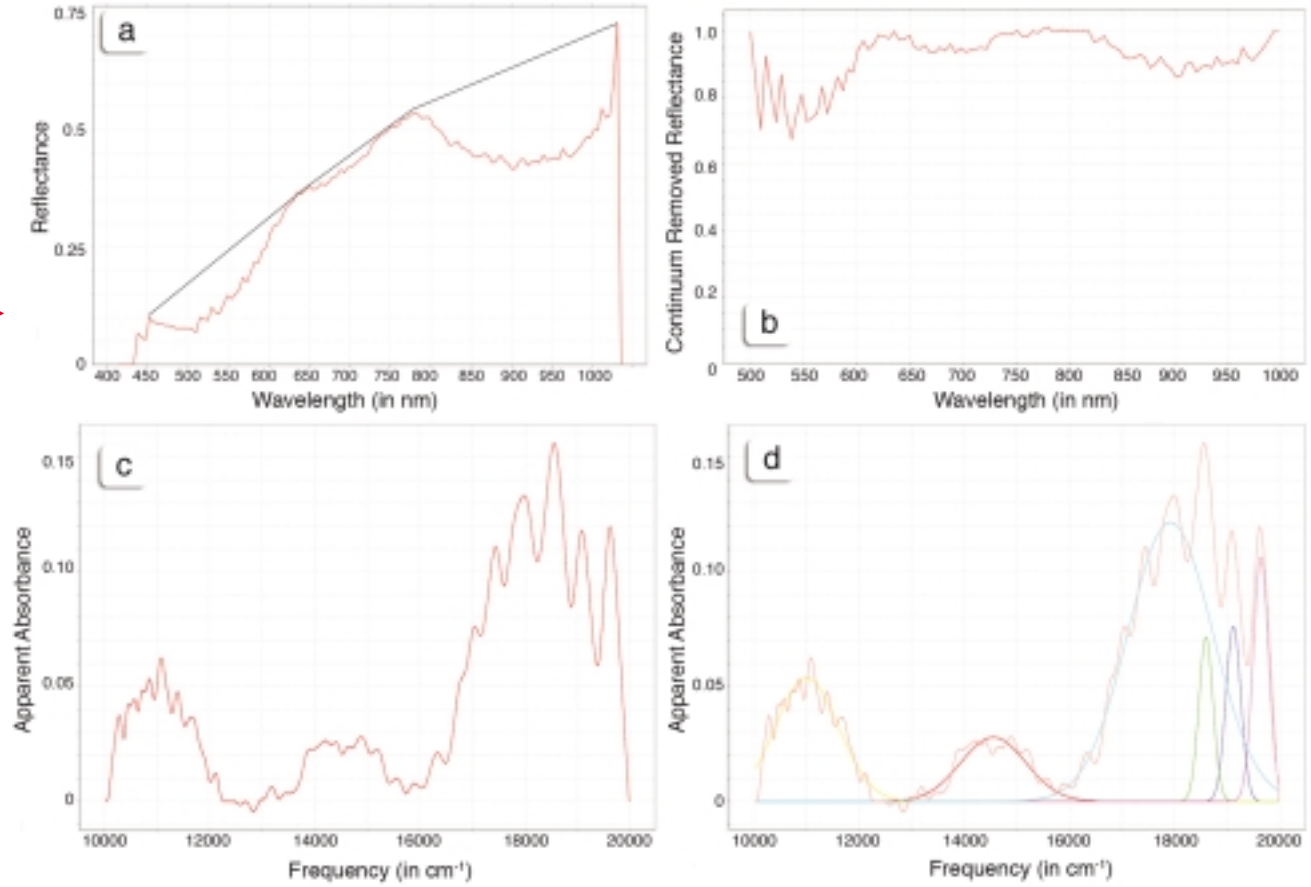

4C

FIG. 8. Summary of the curve-fitting process. (**a**) Original spectrum and straight-line continuum, (**b**) continuum-removed spectrum (subset of original spectrum from 500–1000 nm), (**c**) inverted wavenumber (cm^{-1}) space curve, (**d**) fitted wavenumber space curve. Note the colored Gaussian curves have captured all absorption bands present.

nm due to trigonally distorted octahedral sites. This causes intensification of the $^6A_1 \rightarrow {}^4A_1$ spin-forbidden band at 430 nm and also intensifies an electron pair transition $2[^6A_1 \rightarrow {}^4T_1]$ at 550 nm (Burns, 1993). It is the combination of the 430 and 550 nm absorption bands in hematite that give a "flat line" in this region, rather than the high shoulder observed in the goethite spectra (Fig. 6).

Scheinost *et al*. (1998) pointed out that, because of overlapping band transitions, goethite, maghemite, and schwertmannite could not be discriminated by VNIR spectroscopy. It is only because we have XRD measurements that show goethite in the MARTE cores that we claim to have discriminated goethite in particular.

Data analysis approach

During the MARTE 2-week remote science operations period, the VNIR imaging spectrometer was only used to extract average spectra from small areas of core. To simulate limited data bandwidth conditions, the remote team could only select small regions (up to 10×10 pixels) where they could retrieve imaging spectrometer data. The remote team took some time to adapt to the user interface, and only the simplest of data analysis was carried out. Simple band ratios of spectra allowed limited mineralogical interpretation. Small images were reconstructed toward the end of the 2-week period that showed some promise for Fe-oxide identification.

After the 2-week science operations period, the complete dataset for all the drilled cores was made available to the remote team to analyze by any means available to them. This allowed more complex methods of data analysis to be applied to the data. In particular, the data analysis took place within a prototype spectral analysis suite called "MR PRISM" (Brown and Storrie-Lombardi, 2006). MR PRISM was originally designed to analyze CRISM data (Murchie *et al*., 2007) but is flexible enough to analyze any hyperspectral imaging datasets.

MARTE image cubes were delivered as 5221 separate "frame" files for one core. Each frame was 580 pixels wide and covered 130 bands, or channels, from 413–1035 nm. To analyze the cubes, a full cube was reconstructed in MR PRISM for each core. With each data point, represented by 4 bytes of floating-point numbers, each reconstructed cube was over ($5221 \times 580 \times 130 \times 4$ bytes) 1.57 GB in size—a formidable task for data analysis.

MR PRISM was developed to analyze hyperspectral data cubes in a variety of ways, but the chosen approach for this project was to use an algorithm for absorption band mapping developed for mapping hydroxyl minerals in the short-

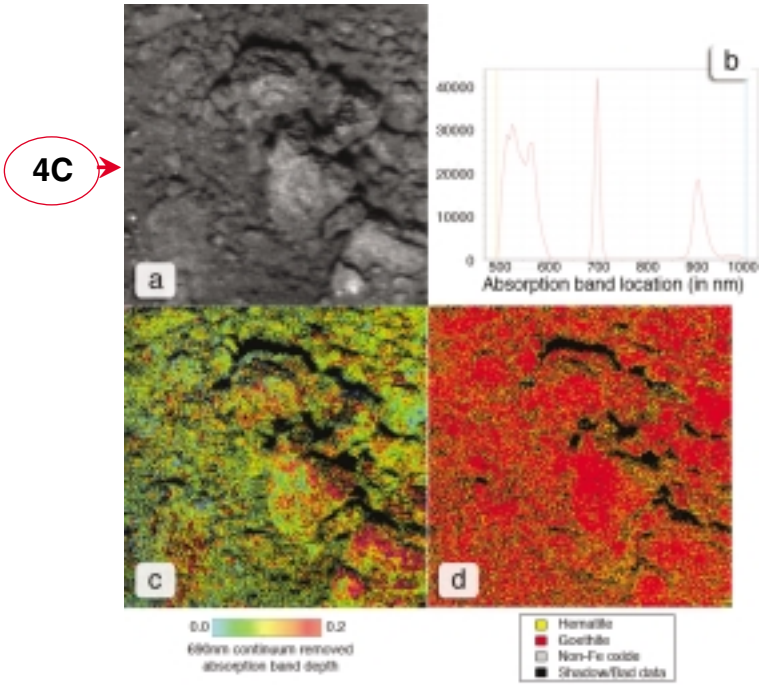

FIG. 9. Core 7 subset analysis results. All images approximately 18 mm across. (**a**) Grayscale image of channel at 567 nm. (**b**) Curve-fitting histogram showing the cumulative total of all absorption bands found. (**c**) 690 nm absorption band depth map. (**d**) Mineral classification map.

wave infrared (Brown *et al*., 2004, 2005, 2006). The modeling approach is discussed further below. This algorithm had not been applied to the VNIR part of the spectrum previously.

To keep the data analysis task manageable, 3 cores with the most morphologically interesting textures were selected, and subsections of these drill cores were chosen where interesting mineral textures and possible compositional gradients were thought to exist. The cores chosen were 7, 23, and 25. Approximate true color images of these cores appear in Fig. 7. Our interpretation of the spectra relied heavily on crystal field theory.

Data analysis technique

We followed an absorption band curve-fitting method, which has previously been applied successfully in the 2000–2500 nm range (Brown, 2006). The steps of the process are outlined in Fig. 8. First, the straight line continuum is removed (subtracted) from the spectrum (Clark *et al*., 1987). The spectrum is then converted to energy (wavenumber) space (Sunshine and Pieters, 1993). Gaussian curves are then generated to match the resultant peaks. The Gaussian parameters are improved in an iterative least squares fitting procedure, until a sufficiently precise match is obtained. We measured errors using a least squares chi-squared value. Each iteration, the chi-squared value was compared to a target value that was computed based on the number of free parameters in our fit. If the difference between chi-square and target value was below a tolerance value (0.001), we considered the least squares run to have converged.

In this way, our analysis resembles that described by Press (1989). The resultant Gaussian curves are converted back into wavelength space and then analyzed with a rule-based expert system in order to produce a mineral map. Parameters of the Gaussian curves such as amplitude, centroid, and width are stored and may be mapped over the processed image to obtain greater insight into the spectral properties of each pixel.

The data analysis technique employed here attempts to model the Fe^{3+} absorption bands in hematite and goethite, since these are the primary minerals occurring in the MARTE drill core. Crystal field theory and experimental data suggest that hematite will have a shorter wavelength for the $^6A_1 \rightarrow {}^4T_1$ transition than goethite (Bishop *et al*., 1993), and the $^6A_1 \rightarrow {}^4T_2$ transition absorption band will be obliterated in hematite due to an intense paired transition $2[^6A_1 \rightarrow {}^4T_1]$ (Fig. 6). Thus, the rule-based system we developed classified a mineral as "hematite" if it possessed a $^6A_1 \rightarrow {}^4T_1$ transition less than 900 nm and goethite if it possessed a $^6A_1 \rightarrow {}^4T_1$ transition greater than 900 nm, in combination with a $^6A_1 \rightarrow {}^4T_2$ transition at around 690 nm.

To learn more about the positions of absorption bands in every analyzed image, our software program also produced a "curve-fitting histogram" that reported the central points of every recognized absorption band in the image. These were summed to create a histogram and are reported below. The advantage of this approach is that, if an unrecognized absorption band is appearing in many of the pixels in the image, it will become apparent as an anomalous peak. We found, during the "fine tuning" of our curve-fitting parameters, that it was invaluable to have immediate knowledge (provided by the histogram) on where in the EM spectrum most absorption band peaks were being found. This allowed us to make decisions on whether to adjust our parameters (and thus include more identified pixels in a mineral map).

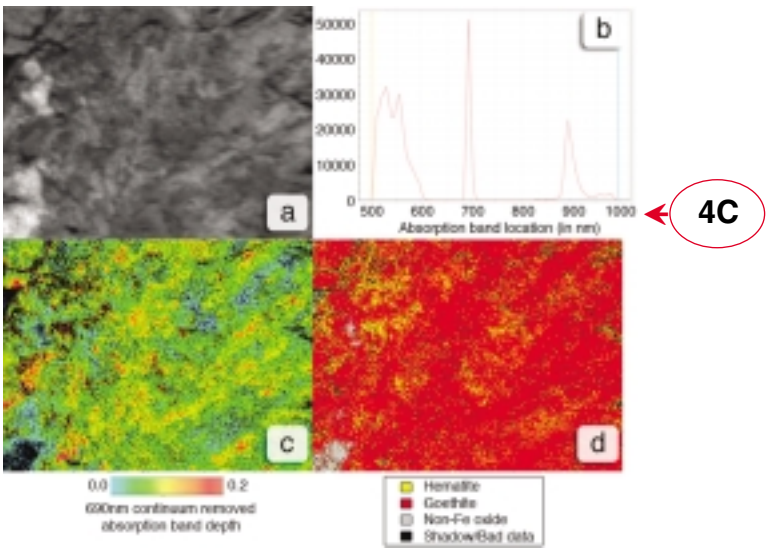

FIG. 10. Core 23 subset 1 analysis results. All images approximately 18 mm across and 14 mm high. (**a**) Grayscale image of channel at 567 nm. (**b**) Curve-fitting histogram showing the cumulative total of all absorption bands found. (**c**) 690 nm absorption band depth map. (**d**) Mineral classification map.

It is important to note that, previously in the literature, authors have reported the central wavelength of $^6A_1 \rightarrow {}^4T_1$ and $^6A_1 \rightarrow {}^4T_2$ features as the minimum of non-continuum-removed spectra. Due to the steep slope of most spectra in the 500–700 nm region, when the continuum is removed, the absorption band center shifts to the right (to higher wavelengths). Thus the figures reported in this paper are approximately 30–40 nm higher than those reported previously in the literature. We decided to take this departure from custom based on the following line of reasoning:

(1) All VNIR spectra, particularly those in the visible, are affected by a strong drop-off in reflectance due to absorption by transition metals.
(2) It is difficult to know the true strength of this absorption and model its effects as a Gaussian shape because the central absorption point of such a shape does not exist. The relevance of Gaussian modeling of this continuum drop-off is, therefore, unjustified and at best unclear. To our knowledge, this has not been previously attempted.
(3) A straight-line (or linear) continuum model of the effects of the strong transition ion drop-off is the most relevant way to compensate for an absorption of variable strength.
(4) It is essential to make some compensation for this strong continuum absorption because of its variability and in order to allow the comparison of weaker bands (such as those discussed in this paper).

We therefore believe that studies that have simply stated the minimum of the band (by eye) are not easy to compare with other results that have differing and uncompensated continuum slopes.

XRD Validation

X-ray diffraction analysis was performed on powdered samples (<45 μm) extracted from Cores 23 and 25 after the mission simulation. Core 7 was not analyzed with XRD. Samples were examined by a PANalytical X'Pert Pro PW 3040/60 diffractometer run under CoKα, at 40 kV, 40 mA, with a scan range 4–80 2θ, step of 0.02, and at 20 s per scan. Goethite and hematite were the dominant Fe-bearing minerals detected in Cores 23 and 25. White material found in both cores was attributed to mica—either as illite or muscovite. Trace amounts of kaolinite and smectite were also detected in Core 23 but not Core 25 (Sutter *et al*., 2008).

Results

Core 7

Core 7 consisted mostly of fine, ochre-red soil, with little visible compositional variation (Fig. 7). Some clumps of material and small pebbles were present. One 400 × 400 pixel subset of Core 7 was chosen for analysis in proximity to a number of small pebbles in the bottom part of the core. The results are shown in Fig. 9. From the mineral map, it can be seen that the scene is full of goethite, with small amounts of more hematitic material that appears to be sprinkled throughout the scene, with no strong preference for the consolidated material in the scene. From the 690 nm absorption band depth map, it can be seen that the strongest 690 nm absorption bands are associated strongly with the competent pebbles (*e.g*., in the lower right corner of the image). It is likely that more highly crystalline goethite within the pebbles is responsible for this effect.

Core 23

Core 23 had the most compositional variety of any cores analyzed during the MARTE experiment. Using XRD, muscovite/illite was found in two locations: (1) in 1 cm wide white-colored pebbles and (2) as a yellow-colored internal veining of red-purple–colored chips (Sutter *et al*., 2008).

Two 400 × 300 pixel subsets of the core were sampled (Fig. 7). The first subset captured a radially streaked part of the core that displayed intriguing texture and color variations. The results of the analysis are shown in Fig. 10. The mineral map shows that small amounts of hematite are clumped together in moderately dark albedo parts of the scene (especially the top left). This is the only core we analyzed where the iron oxide absorption bands revealed strong indications of spatially connected zones of hematite. The mineral mapping also revealed several points on the left hand side of the image that showed no absorption bands and, hence, did not contain iron-bearing minerals. These high-albedo locations were sampled and analyzed by XRD, and most of them contain muscovite/illite (Sutter *et al*., 2008). The 690 nm absorption band depth map in Fig. 10 shows that the strongest absorption bands appear to form linear streaks that go from bottom left to top right. This is in accord with the visible veining relationships characteristic of this part of the core.

The results from an analysis of a second 400 × 300 pixel subset of Core 23 are shown in Fig. 11. The mineral map shows that this area is again predominantly composed of goethite. No patches of hematite were detected, but an intriguing non Fe oxide of low albedo was detected in the top left quadrant of the image (above the shadow). It is not just a shadow or crack, because even shadows that contain Fe oxide show evidence of Fe oxide bands. It is probably not muscovite, due to its relatively low albedo, but we were unable to sample this point and analyze the material with XRD. The absorption band map shows that, even though the whole surface of this competent sample is goethitic, the strongest absorption bands occur in the spatially coherent part of the core surface shown on the left-hand side of the image. It is likely the sharp contact between this high absorption band area and the medium absorption band region are due to a high crystalline matrix in this inclusion.

Core 25

Core 25 displayed an intermediate rock-soil nature, similar to that of Cores 7 and 23. It contained some consolidated material, chiefly in the bottom part of the core (Fig. 7).

We chose to analyze a section of Core 25 that displayed a transition from disaggregated material to more consolidated material. The section analyzed is shown in Fig. 12. The mineral map shows that almost all the scene is goethite, but there are also regions of the more consolidated material that are not Fe-oxide. These appear in the bottom part of Fig. 12. The regions that are not associated with Fe oxide bands are also high in albedo. Similar regions were sampled in Core 25, and they are characterized by a 50/50 mixture of goethite and muscovite/illite (Sutter *et al*., 2008). The areas of the consolidated material that were not high in albedo displayed rela-

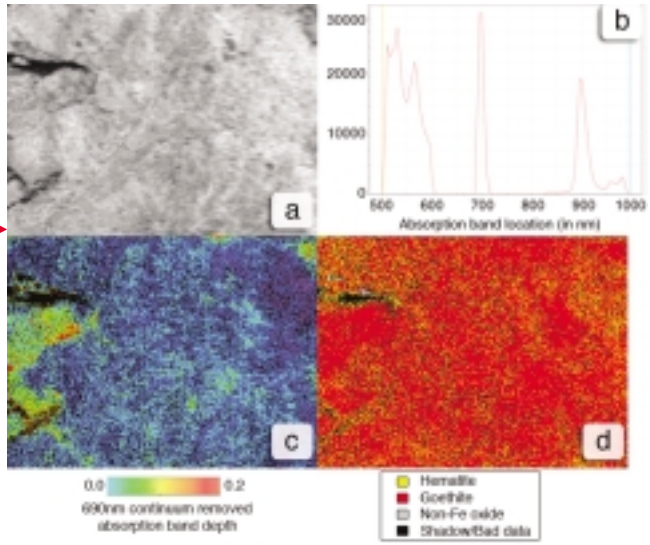

FIG. 11. Core 23 subset 2 analysis results. All images approximately 18 mm across and 14 mm high. (**a**) Grayscale image of channel at 567 nm. (**b**) Curve-fitting histogram showing the cumulative total of all absorption bands found. (**c**) 690 nm absorption band depth map. (**d**) Mineral classification map.

tively deep 690 nm absorption bands, which suggests more crystalline goethite may be present in lower-albedo parts of the consolidated material.

Discussion

Interpretations

The mineral and absorption band maps shown in Figs. 9–12 suggest that most of Cores 7, 23, and 25 were composed predominantly of goethite, with small pockets of hematite and non Fe-oxide material spread throughout parts of these cores, which remained competent after extraction. It is interesting that the most spatially coherent hematite cells occurred in association with a high-albedo non-Fe oxide we identified as muscovite/illite (Sutter *et al*., 2008). One possibility is that the hematite may have formed from goethite as an oxidative by-product in a less-reducing hydrothermal reaction. Alternatively, hematite may have formed by reorganization of ferrihydrite. Note that, due to the band matching technique we adopted, it is statistically more likely that, in some regions where there are shadows or bad data, hematite will be "detected" in the edges of these areas since hematite detections only require the identification of 1 absorption band, whereas goethite detections require 2. Thus, hematite detections on the edges of "no data" or "shadowed" regions require careful examination.

The final core analyzed, Core 25, appeared to contain consolidated material that is a mixture of goethite and high-albedo non–Fe oxide. From post-mission XRD analysis, we concluded that the non–Fe oxide is muscovite or some other phyllosilicate material. We interpret this material as a vestige of highly penetrative hydrothermal alteration, with goethite and phyllosilicate-rich zonal alteration regions.

In this study, we made several new findings in the field of VNIR spectroscopy. These were mostly facilitated by the absorption band data analysis method, which is designed to explore the data and uncover hidden details when a numerical description of the spectral bands is available.

(1) **Constraints on the spread of Fe-oxide absorption bands**. Analysis of all 3 cores resulted in similar absorption band histograms (shown in Figs. 9–12), despite the variation in soil-rock ratios and mineral composition. It cannot be taken as proven that this will always be the case, but this finding demonstrates the general "stability" of Fe-oxide bands.

(2) **Nature of the 690 nm $^6A_1 \rightarrow {}^4T_2$ feature distribution**. The tight spread of the 690 nm feature makes it useful for goethite detection. Scheinost *et al*. (1998) pointed out that ferrihydrite and feroxyhite are identifiable in the VNIR because both display this feature at wavelengths greater than 700 nm. However, we found no evidence for these minerals in our samples. We found absorption band depth maps of this feature to be extremely rich in spatial information, and we attribute this to the occurrence of patches of crystalline goethite within the examined cores.

(3) **Nature of the 900 nm $^6A_1 \rightarrow {}^4T_1$ distribution**. We were able to use the T_1 900 nm feature as a compositional index, with goethite-rich regions displaying a central wavelength >900 nm, and goethite-poor regions showing a T_1 feature <900 nm. This has been reported by other authors (Cudahy and Ramanaidou, 1997); however, we applied it, in this study, to a real-life scenario with an imaging spectrometer.

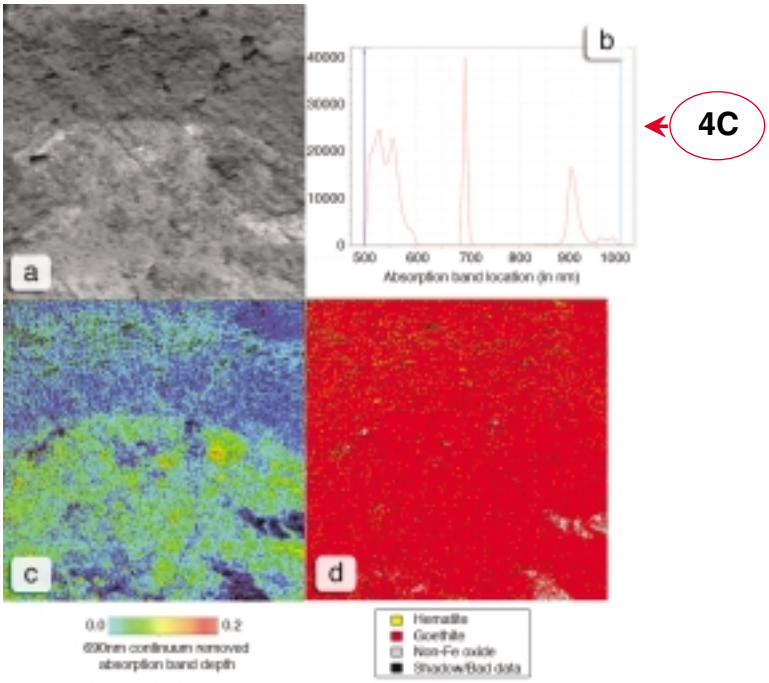

FIG. 12. Core 25 subset analysis results. All images approximately 18 mm across. (**a**) Grayscale image of channel at 567 nm. (**b**) Curve-fitting histogram showing the cumulative total of all absorption bands found. (**c**) 690 nm absorption band depth map. (**d**) Mineral classification map.

(4) **Ability to detect non-Fe-oxide materials**. It is a challenging matter to identify the presence of non-Fe-oxide material in the VNIR by way of simple (or complex) band ratios, false color images, and (especially) principle components analysis. We have demonstrated the ability of this method to discriminate automatically both high- and low-albedo non-Fe-bearing material based on the absence of strong absorption bands.

Experimental limitations

VNIR spectroscopy is inherently limited to observing the nature of transition metal electronic absorption bands. As such, the presence of silicates, phyllosilicates, amphiboles, pyroxenes, sulfates, and carbonates can, for the most part, only be estimated. We consider this apparatus and its performance on the MARTE project a successful proof of concept. A future Mars drilling rig should be equipped with an instrument that can cover at least to the shortwave infrared (up to 2500 nm) and possibly beyond.

Future work

At this time, we are unable to capitalize on the (possibly bimodal) distribution of absorption bands around 550 nm. With our current absorption band implementation, most pixels in our study showed at least two absorption bands between 500 and 600 nm. We were unable to recognize a significant link to composition due to two factors: (1) Fe oxides have several overlapping bands in this region (Scheinost *et al*., 1998) and (2) The MARTE VNIR imaging spectrometer has lower signal-to-noise characteristics in this part of the spectrum. In the event that an imaging spectrometer is to be selected for drill-core analysis on a future Mars mission, higher signal-to-noise characteristics should be considered so as to allow automated band analyses over a broader wavelength (or wavenumber) range, as was attempted here.

Conclusion

We have summarized the design and construction of the VNIR imaging spectrometer and described a unique absorption band modeling method that was used for data analysis. In so doing, we have highlighted the usefulness of this technique for differentiating between goethite-hematite mixtures and for recognition of non-Fe-bearing minerals. Although this information is only of indirect use in the search for life in subsurface drill cores, it can give invaluable contextual information on the mineralogical environment. A hyperspectral spectrometer that covers at least the VNIR will be an essential part of a future Mars remote drilling astrobiology mission.

Acknowledgments

We would like to thank the entire MARTE Team, especially the Principal Investigator, Dr. Carol Stoker, for their commitment and camaraderie during the project. We would also like to thank Dr. Ted Roush and two anonymous referees for their thoughtful reviews.

Abbreviations

CRISM, Compact Reconnaissance Imaging Spectrometer for Mars; MARTE, Mars Astrobiology Research and Technology Experiment; MR PRISM, a prototype spectral analysis suite; obf, order-blocking filter; VNIR, Visible–Near Infrared; XRD, X-ray diffraction.

References

Bethe, H. (1927) Über die Streuung von Elektronen an Krystallen. *Naturwissenschaften* 15:786–788.

Bishop, J.L., Pieters, C.M., and Burns, R.G. (1993) Reflectance and Mössbauer-spectroscopy of ferrihydrite-montmorillonite assemblages as Mars soil analog materials. *Geochim. Cosmochim. Acta* 57:4583–4595.

Brown, A.J. (2006) Spectral curve fitting for automatic hyperspectral data analysis. *IEEE Transactions on Geoscience and Remote Sensing* 44:1601–1608.

Brown, A.J. and Storrie-Lombardi, M.C. (2006) MR PRISM—an analysis tool for the CRISM. In *Proceedings of SPIE Optics and Photonics*, SPIE, Bellingham, WA.

Brown, A.J., Cudahy, T.J., and Walter, M.R. (2004) Short wave infrared reflectance investigation of sites of palaeobiological interest: applications for Mars exploration. *Astrobiology* 4:359–376.

Brown, A.J., Walter, M.R., and Cudahy, T.J. (2005) Hyperspectral imaging spectroscopy of a Mars analog environment at the North Pole Dome, Pilbara Craton, Western Australia. *Australian Journal of Earth Sciences* 52:353–364.

Brown, A.J., Cudahy, T.J., and Walter, M.R. (2006) Hydrothermal alteration at the Panorama Formation, North Pole Dome, Pilbara Craton, Western Australia. *Precambrian Res*. 151:211–223.

Burns, R.G. (1993) *Mineralogical Applications of Crystal Field Theory*, 2nd ed., Cambridge University Press, Cambridge.

Clark, R.N., King, T.V.V., and Gorelick, N. (1987) Automatic continuum analysis of reflectance spectra. In *Proceedings of the 3rd Airborne Imaging Spectrometer Data Analysis Workshop*, JPL Publication 87-30, Jet Propulsion Laboratory, Pasadena, CA, pp 138–142.

Clark, R.N., Swayze, G.A., Wise, R., Livo, K.E., Hoefen, T.M., Kokaly, R.F., and Sutley, S.J. (2003) *USGS Digital Spectral Library splib05a*, USGS Open File Report, US Geological Survey, Reston, VA.

Cudahy, T.J. and Ramanaidoum, E.R. (1997) Measurement of hematite:goethite ratio using visible and near-infrared reflectance spectroscopy in channel iron deposits, Western Australia. *Australian Journal of Earth Sciences* 44:411–420.

Davis, C.O., Bowles, J., Leathers, R.A., Korwan, D., Downes, T.V., Snyder, W., Rhea, W., Chen, W., Fisher, J., Bissett, P., and Reisse, R.A. (2002) Ocean PHILLS hyperspectral imager: design, characterization, and calibration. *Opt. Express* 10:210–221.

Fernández-Remolar, D., Rodriguez, N., Gomez, F., and Amils, R. (2003) The geological record of an acidic environment driven by iron hydrochemistry: the Tinto River system. *J. Geophys. Res*. 108, doi:10.1029/2202JE001918.

Fernández-Remolar, D.C., Morris, R.V., Gruener, J.E., Amils, R., and Knoll, A.H. (2005) The Río Tinto Basin, Spain: mineralogy, sedimentary geobiology, and implications for interpretation of outcrop rocks at Meridiani Planum, Mars. *Earth Planet. Sci. Lett*. 240:149–167.

Hunt, G.R. (1977) Spectral signatures of particular minerals in the visible and near infrared. *Geophysics* 42:501–513.

Hyvarinen, T.S., Herrala, E., and Dall'Ava, A. (1998) Direct sight imaging spectrograph: a unique add-in component brings spectral imaging to industrial applications. In *Digital Solid*

State Cameras: Designs and Applications, SPIE, Bellingham, WA, pp 165–175.

Kappus, N., Aldrich, W., Resmini, R.C., and Mitchell, P. (1996) The flexible HYDICE sensor's first year of operation. In *Proceedings of the 11th Thematic Conference and Workshops on Applied Geologic Remote Sensing, Las Vegas,* February 27–29, 1996, pp 433–441.

Murchie, S., Arvidson, R., Bedini, P., Beisser, K., Bibring, J.-P., Bishop, J., Boldt, J., Cavender, P., Choo, T., Clancy, R.T., Darlington, E.H., Des Marais, D., Espiritu, R., Fort, D., Green, R., Guinness, E., Hayes, J., Hash, C., Heffernan, K., Hemmler, J., Heyler, G., Humm, D., Hutcheson, J., Izenberg, N., Lee, R., Lees, J., Lohr, D., Malaret, E.T.M., McGovern, J.A., McGuire, P., Morris, R., Mustard, J., Pelkey, S., Rhodes, E., Robinson, M., Roush, T., Schaefer, E., Seagrave, G., Seelos, F., Silverglate, P., Slavney, S., Smith, M., Shyong, W.-J., Strohbehn, K., Taylor, H., Thompson, P., Tossman, B., Wirzburger, M., and Wolff, M. (2007) Compact Reconnaissance Imaging Spectrometer for Mars (CRISM) on Mars Reconnaissance Orbiter (MRO). *J. Geophys. Res*. 112, doi:10.1029/2006JE002682.

Press, W.H., Flannery, B.P., Teukolsky, S.A., and Vetterling, W.T. (1989) *Numerical Recipes in Pascal*, Cambridge University Press, New York.

Scheinost, A.C., Chavernas, A., Barron, V., and Torrent, J. (1998) Use and limitations of second-derivative diffuse reflectance spectroscopy in the visible to near-infrared range to identify and quantify Fe oxide minerals in soils. *Clays and Clay Miner*. 46:528–536.

Schermerhorn, L.J.G. (1970) The deposition of volcanics and pyritite in the Iberian pyrite belt. *Mineralium Deposita* 5:273–279.

Stoker, C.R., Cannon, H.N., Dunagan, S.E., Lemke, L.G., Glass, B.J., Miller, D., Gomez-Elvira, J., Davis, K., Zavaleta, J., Winterholler, A., Roman, M., Rodriguez-Manfredi, J.A., Bonaccorsi, R., Bell, M.S., Brown, A., Battler, M., Chen, B., Cooper, G., Davidson, M., Fernández-Remolar, D., Gonzales-Pastor, E., Heldmann, J.L., Martínez-Frías, J., Parro, V., Prieto-Ballesteros, O., Sutter, B., Schuerger, A.C., Schutt, J., and Rull, F. (2008) The 2005 MARTE robotic drilling experiment in Río Tinto, Spain: objectives, approach, and results of a simulated mission to search for life in the martian subsurface. *Astrobiology* 8:xxx–xxx.

Sunshine, J.M. and Pieters, C.M. (1993) Estimating modal abundances from the spectra of natural and laboratory pyroxene mixtures using the Modified Gaussian Model. *J. Geophys. Res*. 98:9075–9087.

Sutter, B., Brown, A., and Stoker, C.R. (2008) Visible-near infrared spectroscopy of drill core samples from Río Tinto, Spain: results from the 2005 Mars Astrobiology Research and Technology Experiment (MARTE) drilling exercise. *Astrobiology* 8:xxx–xxx.

Address reprint requests to:
Adrian J. Brown
SETI Institute
515 N. Whisman Road
Mountain View, CA 94043

E-mail: abrown@seti.org